



RESEARCH ARTICLE OPEN ACCESS

A Comparative Study of Recombination Mechanisms and Long-Term Outdoor Degradation in Perovskite Solar Cells and Modules Including Self-Assembled Monolayers

Silvia Delgado-Rodríguez¹ | Gonzalo del Pozo¹ | Pedro Contreras¹ | Belén Arredondo¹ | Sujith Vishwanathreddy^{2,3,4} | Jonathan Parion^{2,3,4,5} | Santhosh Ramesh^{2,3,4} | Tom Aernouts^{2,3,4} | Aranzazu Aguirre^{2,3,4} | Beatriz Romero^{1,6}

¹Escuela Superior de Ciencias Experimentales y Tecnología, Universidad Rey Juan Carlos, Móstoles, Madrid, Spain | ²Thin Film PV Technology, Imec, imo-imomec, Genk, Belgium | ³Hasselt University, imo-imomec, Hasselt, Belgium | ⁴EnergyVille, imo-imomec, Genk, Belgium | ⁵Department of Electronics and Information Systems, Ghent University, Zwijnaarde, Belgium | ⁶Instituto de Investigación de Tecnologías para la Sostenibilidad, Universidad Rey Juan Carlos, C/Tulipán s/n, Móstoles, Spain

Correspondence: Beatriz Romero (beatriz.romero@urjc.es)

Received: 29 March 2025 | **Revised:** 23 May 2025 | **Accepted:** 27 May 2025

Funding: Agencia Estatal de investigación, Grant/Award Numbers: PID2023-148746OB-I00, TED2021-131807A-I00; Universidad Rey Juan Carlos, Grant/Award Number: 2023/SOLCON-131819; fonds wetenschappelijk onderzoek, Grant/Award Number: 1S01525N

Keywords: characterization | outdoor degradation | perovskite solar cells | self-assembled monolayers | temperature

ABSTRACT

Perovskite solar cells are one of the most promising photovoltaic technologies in the last decades. Inverted (p-i-n) cells using NiO_x as hole-transport layer (HTL) have gained attention due to their easy fabrication methods and high stability, although they often exhibit reduced efficiencies due to non-optimized energy-level alignment. To address this issue, different approaches have been developed, such as the use of self-assembled monolayers (SAMs) on top of the HTL. Herein, a comparative study between regular p-i-n cells and cells using Me-PACz as an SAM on top of NiO_x is presented. Devices with SAM exhibit enhanced open-circuit voltage and efficiency. Temperature DC and AC characterization reveals that the incorporation of SAM reduces recombination at the interface, as seen from the comparison of the perovskite bandgap (1.6 eV) and carrier activation energy ≈ 1.1 and ≈ 1.59 eV for reference and SAM, respectively. Finally, an outdoor degradation experiment with minimodules has been conducted. The experiment spanned for more than 500 days, and results show that minimodules with SAM were less stable than those based on the reference layer structure. This is due to a severe decrease in the short-circuit current, which could be attributed to a deterioration of the SAM spacer.

1 | Introduction

In the last decade, the field of photovoltaics has been revolutionized by the advent of perovskite solar cells (PSC). These novel devices, based on hybrid halide perovskite semiconductors as active layer, have demonstrated a rapid increase in efficiency, surpassing many established solar technologies in a remarkably short period [1]. Since the first reports of PSCs, more than a decade ago, their efficiency has skyrocketed from initial values of around 3% [2] in 2009 to over 26% [3] today, rivaling that

of traditional silicon-based cells. This outstanding improvement is largely due to the unique properties of hybrid metal halide perovskite materials. They have excellent light absorption characteristics and high carrier mobilities and can be processed at low temperatures, which makes them highly suitable to be used in solar cells. Moreover, the ability to tune the perovskites bandgap by chemical engineering facilitates the realization of tandem solar cells with even higher efficiencies. In addition to their impressive performance, PSCs offer several advantages over other photovoltaic technologies such as low-cost manufacture

This is an open access article under the terms of the [Creative Commons Attribution](https://creativecommons.org/licenses/by/4.0/) License, which permits use, distribution and reproduction in any medium, provided the original work is properly cited.

© 2025 The Author(s). *Solar RRL* published by Wiley-VCH GmbH.

procedure and materials compared to other thin-film technologies. Furthermore, their flexibility, transparency, and lightweight make them ideal for integration into building materials or for applications in portable electronic devices [4]. However, despite these promising features, PSCs still face significant challenges that need to be addressed. These challenges include scalability constraints, the presence of lead in most high-efficiency devices and particularly stability concerns. In fact, stability is a major issue in halide perovskite since these materials are vulnerable to ion migration, mainly of iodine (I_2) and iodine vacancies [5]. A tiny amount of these defects can trigger chemical reactions that compromise the stability of the device.

Regarding the layer structure, PSC can be fabricated in two main configurations: regular or standard (n-i-p) and inverted (p-i-n). Though higher efficiencies have been traditionally achieved using standard configuration, currently both structures present similar power conversion efficiency (PCE) values [6]. Besides, the use of high-temperature processes (i.e. 450°C for TiO_x) and the more expensive materials (such Spiro-OMeTAD and Au) needed for n-i-p configuration are major drawbacks for their development. On the contrary, p-i-n PSCs have gained significant interest because they can be produced at low temperatures, remain stable in ambient air, and offer potential applications in tandem solar cells [7, 8]. To accelerate their commercialization, recent research on inverted PSCs has been focused on optimizing the HTL to improve efficiency and stability. Self-assembled monolayers (SAMs) of organic molecules are considered an interesting substitute for traditional single-carrier transport layers [9, 10]. SAMs can serve not only as HTL but also as an effective interface layer between the perovskite active layer and the charge-transport layers. They can adjust the energy level alignment between the active layer and HTL resulting in an enhanced open-circuit voltage (V_{OC}) [11], passivate trap states [12], and improve the morphology of the perovskite film [13], thus leading to a higher device efficiency. Moreover, SAMs can provide a barrier against moisture and ion migration, two major causes of PSC degradation, thereby enhancing device stability [14–16]. Therefore, the integration of SAMs into PSCs provides a powerful tool for the optimization of device performance and lifetime.

Regarding nickel oxide (NiO_x), it has emerged as one of the most interesting HTL for p-i-n PSCs due to its attractive characteristics. These include a low material cost, suitability for multijunction structures and scalability [17, 18], high transparency, and high carrier mobility [19]. However, NiO_x -based PSCs exhibit low V_{OC} due to the lower energy-level alignment and high recombination at the interface [20, 21]. Tutundzic et al. have demonstrated that the use of the carbazole-based SAM Me-4PACz on top of the NiO_x reduces the valence band level and minimizes the energy-level misalignment between the perovskite active layer and the HTL (NiO_x) [22]. Liu et al. have demonstrated a certified 26.54% PCE for inverted PSCs by co-assembling a multiple carboxylic acid with Me-4PACz. After more than 2,400 h of continuous operation under 1 sun in ambient air, encapsulated devices maintained more than 96% of their initial efficiency [23]. Moreover, some studies report an enhancement of the stability when using the NiO_x /SAMs bilayer structure at temperatures exceeding 65°C for indoor short-term experiments (around 500 h) [24].

In this work, inverted PSCs using the hole selective bilayer NiO_x /SAM have been fabricated and characterized at different illumination levels (from 0.1 suns up to 1 suns) and at different temperatures (from -20°C up to 60°C). Similar devices without the SAM layer have been developed and characterized as reference cells. Ideality factors have been extracted for both types of devices in their pristine state, revealing that SAM improves the selectivity of the contacts and reduces carrier recombination at the interface. From J - V characterization at different temperatures, the PCE temperature coefficient (T_{PCE}) was extracted, yielding a value of 0.002°C^{-1} . This is a remarkable value compared to other traditional technologies such as silicon or GaAs-based solar cells, confirming that PSCs are good candidates to operate at high-temperature or high-irradiated locations. An activation energy of 0.55 eV has been obtained from impedance spectroscopy (IS) measurements at different temperatures, which is higher than the values obtained in methylammonium lead iodide (MAPI) [5, 25]. Some authors have previously attributed this to the incorporation of the inorganic Cs cation [26], but a more recent work suggests that it might also be related to a reduced recombination capability of these ions at the interfaces [27]. Finally, minimodules based on both structures have been degraded following ISOS-O2 protocol for more than 18 months. Despite benefits of using SAM in the pristine state, these minimodules exhibit a more pronounced degradation in the long-term, driven by a stronger decrease of the short-circuit current than reference modules.

2 | Experimental Method

2.1 | Fabrication

We have fabricated small-area (0.13 cm^2) p-i-n PSCs with the reference structure, ITO/ NiO_x /CsFAPbIBr/LiF/ C_{60} /BCP/ITO/Cu, including SAMs on top of the NiO_x HTL and ITO/ NiO_x /Me-4PACz/CsFAPbIBr /LiF/ C_{60} /BCP/ITO/Cu. The fabrication procedure is thoroughly explained in ref. [22]. Due to the sensitivity of the Me-4PACz formation on the NiO_x layer, special measures were taken to mitigate the impact of variables such as roughness, air exposure, and ambient humidity. Mild sputtering conditions were employed and surface treatment along with SAM deposition in an inert environment to ensure high quality and reproducibility. Each substrate contains 12 independent cells.

The modules were fabricated with the same layer stack with interconnections formed through laser scribing using the P1-P2-P3 approach [22]. The aperture active area of the modules is 4 cm^2 , with seven cells interconnected in series, thus resulting in the summation of the voltage of each individual cell.

2.2 | Characterization

Current density–voltage (J - V) characterization was performed using a Xenon Lamp solar simulator (Oriel Sol3A class AAA) with 1000 W m^{-2} illumination with an AM1.5G spectrum. The temperature was controlled by a fan, ensuring that the devices remained at room temperature (RT) during the measurements. J - V curves were measured with an Autolab potentiostat/galvanostat

PGSTAT204, in reverse mode (from V_{OC} to J_{SC}) and using a 20 mV s^{-1} scan rate.

IS measurements were performed under different light intensities (from 1 to 0.1 sun) at V_{OC} . Frequency ranged between 1 MHz and 0.1 Hz, applying a small signal of 20 mV amplitude. Experimental data were fitted using ZView 3.2 software.

Temperature measurements were performed inside a chamber with N_2 atmosphere to avoid condensed water at temperatures below 0°C . The temperature was controlled using a Peltier thermal plate located at the base of the stage and an Instec mK2000 temperature controller. Although the actual intensity of the solar simulator is 1 sun, there is approximately a 15% reduction due to light reflection and absorption losses from the stage window. Therefore, the efficiency obtained in the temperature experiment is underestimated by around 15%.

2.3 | Outdoor Degradation

Two degradation experiments have been carried out following ISOS-O2 protocol [28] in Madrid (coordinates: 40.334, -3.883). The first experiment started on the 21st July and the second experiment began on the 24th November 2023, and both were running until the 28th January 2025. J - V curves have been monitored for each module in an experimental outdoor setting consisting of a dual-axis automatic sun tracker and a National Instruments PXIe-4139 Source Measurement Unit, coupled to a National Instruments PXI-2527 32-channel multiplexer. All modules were kept at open-circuit conditions between

measurements. Solar radiation components (direct, diffuse, and global in both horizontal and 2-axis tracking planes) have been constantly monitored via a Kipp & Zonen Solys2 GPS-based sun tracker equipped with Kipp & Zonen CMP6 and EPLAB SPP pyranometers, together with a Kipp & Zonen CHP1 pyrliometer. Outdoor weather conditions (temperature, relative humidity, atmospheric pressure, wind data, and precipitation) have also been acquired using Alhborn FHAD and Thies Clima sensor modules.

3 | Results and Discussion

3.1 | DC Characterization at RT

Figure 1 shows solar cell parameters, J_{SC} , V_{OC} , fill factor (FF) and PCE for the fabricated devices: six substrates (with 12 devices in each substrate) with the reference structure and five substrates including SAM. The results demonstrate that the initial efficiency is higher for devices using SAM ($\approx 14\%$) than for reference ones ($\approx 11\%$) mainly due to a higher V_{OC} (1.1 V vs 0.95 V respectively). This increase in V_{OC} was expected, since it is well known that the incorporation of SAM between the perovskite and the HTL improves the energy alignment between the highest occupied molecular orbital (HOMO) of the HTL bilayer (NiO_x/SAM) and the valence band (VB) of the perovskite. The effect of including SAM results in a decrease of the HOMO level of the HTL bilayer from -5.0 to -5.2 eV and thus the Fermi level from -4.2 to -4.45 eV (see Figure 2) [29], approaching the Fermi level of the perovskite (-4.72 eV) and leading to an increase of V_{oc} . Moreover, minimizing the energy offset between HOMO level

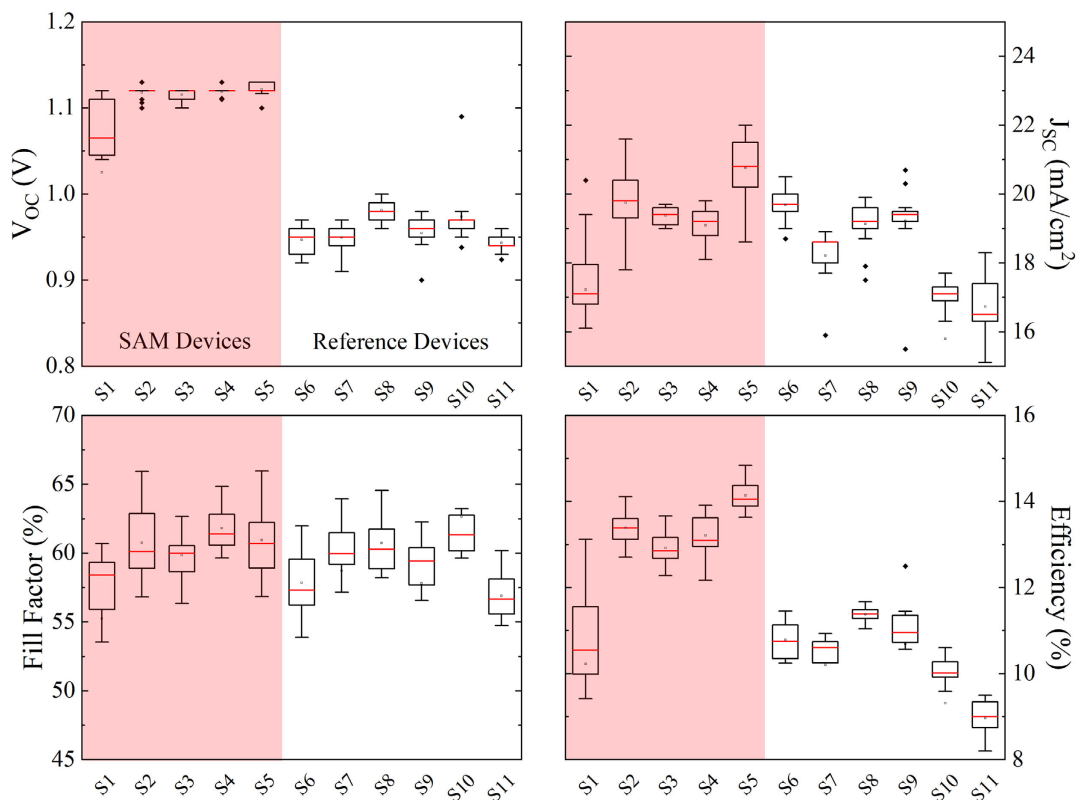


FIGURE 1 | Solar cells parameters: J_{SC} , V_{OC} , FF, and efficiency for all the fabricated devices, with and without SAM.

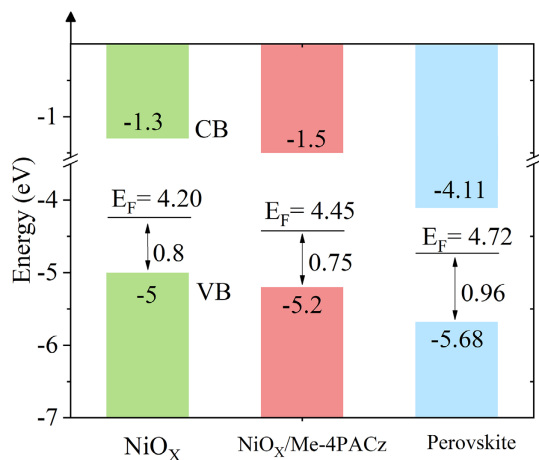


FIGURE 2 | Energy levels of the HTLs (NiO_x , $NiO_x/Me-4PACz$) and the perovskite [29].

of SAM and VB of the perovskite results in a reduction of carrier energy losses, which leads to a more efficient charge carrier extraction [30]. Furthermore, this increase in V_{OC} does not come at the expense of a decrease in the other characteristic parameters. In particular, this balance between increasing V_{OC} and maintaining the FF and J_{SC} is achieved, not only by enhancing energy level alignment, but also by reducing defect density, and promoting rapid hole extraction at the SAMs/perovskite interface [24].

Four cells of each type have been selected to be characterized at different light intensities, from 0.1 suns up to 1 sun. Figure 3 shows the illumination dependence of the four $J-V$ parameters. As expected, J_{SC} depends linearly on the light intensity, with α being a phenomenological parameter, with value close to 1 in both cases (being $J_{SC} = A \times P_{INC}^\alpha$), while V_{OC} has a logarithmic

dependence. The slope of V_{OC} vs light intensity is 79 and 52 $mV \text{ dec}^{-1}$ for SAM and reference cells respectively. Moreover, V_{OC} of the reference cell saturates at high irradiation levels indicating the presence of non-selective contacts. In addition, the ideality factor obtained from the logarithmic dependence of V_{OC} vs light is plotted in Figure 3 inset. Reference devices exhibit a lower ideality factor, below 1, which, together with the saturation of V_{OC} at high light intensities, indicates the dominance of surface recombination in the presence of non-selective contacts. On the other hand, cells with SAM exhibit a higher ideality factor (≈ 1.4). According to P. Capriolo [31] and W. Tress [32], the increase of the ideality factor, when incorporating an SAM in the device, implies a reduction of the interface recombination, which results in an increase of the SRH recombination rate in the bulk. Other authors [33] suggest that recombination at interfaces with improved energy level alignment results in an increase of the ideality factors. However, in our case, activation energy obtained from temperature characterization will confirm that recombination in SAM devices is governed by the bulk. In this sense, it has been shown that SAM layer improves the performance of PSCs since it reduces interface recombination between HTL and perovskite, which yields to an improved open circuit voltage. Finally, FF strongly decreases with light intensity for both types of devices which is attributed to the high series resistance value (higher than 100 Ω , see Figure S1) in agreement with results shown in [33].

3.2 | AC Characterization at RT

Figure 4 shows IS measurements for devices with and without SAM at V_{OC} for different light intensities at RT and Figure 5 shows the low-, medium-, and high-frequency circuitual parameters for both types of devices. Spectra show two clearly differentiated arcs at low frequency (0.1 Hz–1 KHz) and at high

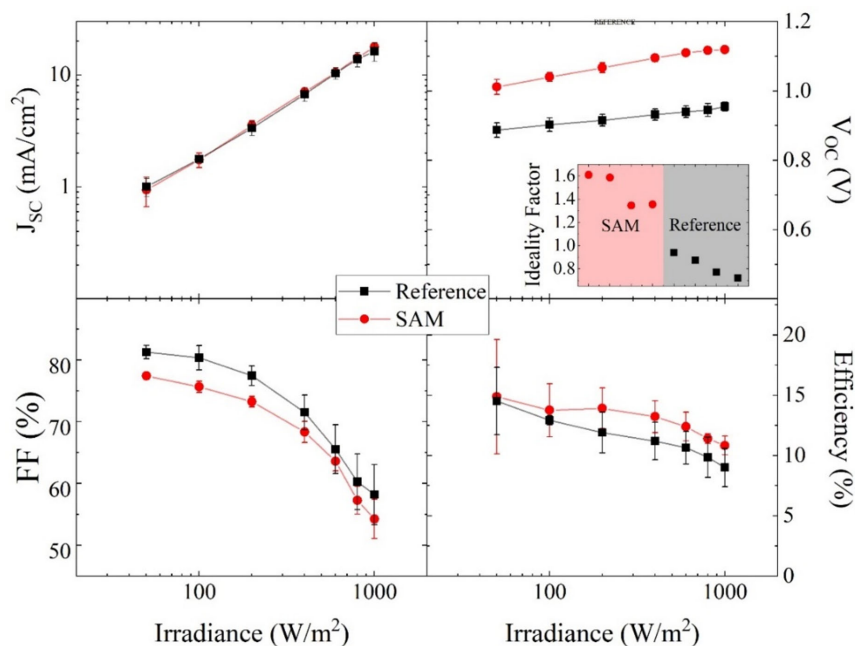


FIGURE 3 | Solar cell parameters versus illumination (from 0.1 to 1 sun) for reference and SAM devices. Inset shows the ideality factor for 8 devices (4 reference and 4 with SAM) obtained from the dependence of V_{OC} with light intensity.

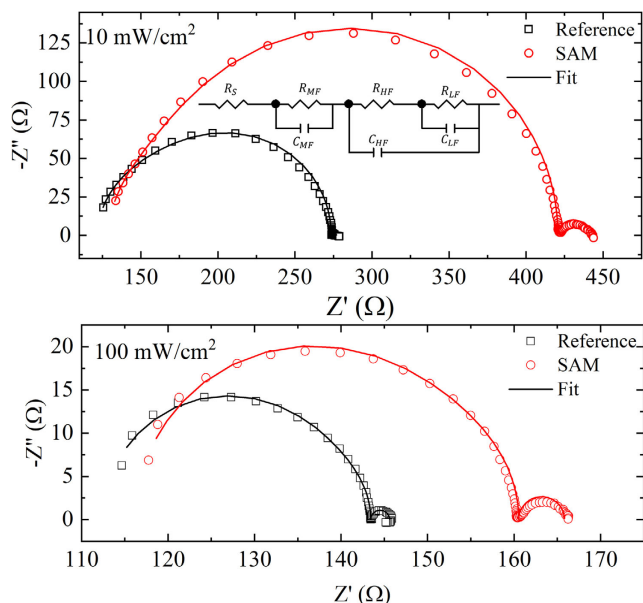


FIGURE 4 | Cole–Cole diagrams for reference and SAM devices at 10 mW cm^{-2} (up) and at 100 mW cm^{-2} (bottom). Symbols are experimental impedance, and solid lines show the best fits using the circuitual model shown in the inset.

frequency (1 kHz–1 MHz). However, observing the high-frequency arc in detail, we can note that it is composed of two overlapped arcs (1–100 kHz and 100 kHz–1 MHz). Therefore, in order to fit the whole spectra we have used the Voigt–Matryoshka circuit [34]. In PSCs, low-frequency arc is typically associated to ion migration. Iodide ions (I^-) are the most probable migrating species in formamidinium lead Iodide-based PSC [5]. At V_{OC} , this species migrates and accumulates at the HTL/perovskite interface forming a double layer. This double

layer hinders efficient charge extraction since it screens the applied electric field [35]. In this work, reference cells show lower resistances and higher low-frequency capacitances than SAM devices. A lower C_{LF} implies diminished ion migration and, consequently, less ion accumulation at the perovskite/HTL interface in devices incorporating SAM [36]. A higher R_{LF} suggests a hampered ionic transport in the SAM cells [36]. Alternatively, in the medium- and high-frequency regimes, the resistances R_{MF} and R_{HF} are associated with the diameter of the larger semicircle depicted in the Cole–Cole plot of Figure 4. Under 1 sun illumination, the diameters (x-axis) of the large semicircles are 140 and 160Ω for the reference and SAM samples, respectively. These values correspond to the sum of R_{MF} and R_{HF} in Figure 5, which is presented on a logarithmic scale. More specifically, R_{HF} and R_{MF} are related to carrier recombination processes. The slightly higher values of R_{HF} and R_{MF} observed in the SAM sample indicate a somewhat reduced charge recombination. Additionally, the ideality factor can also be estimated from the slope of R_{MF} , yielding values of 0.4 and 1.04 for the reference and SAM samples, respectively. These values follow the same trend as the ideality factors obtained from V_{OC} (inset Figure 3) and confirm that carrier recombination is more pronounced in reference samples. Previous studies have indicated that the medium-frequency feature is associated with an ion-modulated recombination rate within the perovskite bulk. These studies propose that a minor population of ‘excess ions’ serves to neutralize small electronic charges in the perovskite layer at time scales approximately 200 times faster than ion migration [37].

On the other hand, high-frequency capacitance (C_{HF}) is associated with geometrical capacitance and remains nearly constant with the illumination level in both samples. Under dark conditions, the permittivity of the perovskite layer, derived from this capacitance, yields values of 42.3 and 35.4 for the reference and SAM cells, respectively.

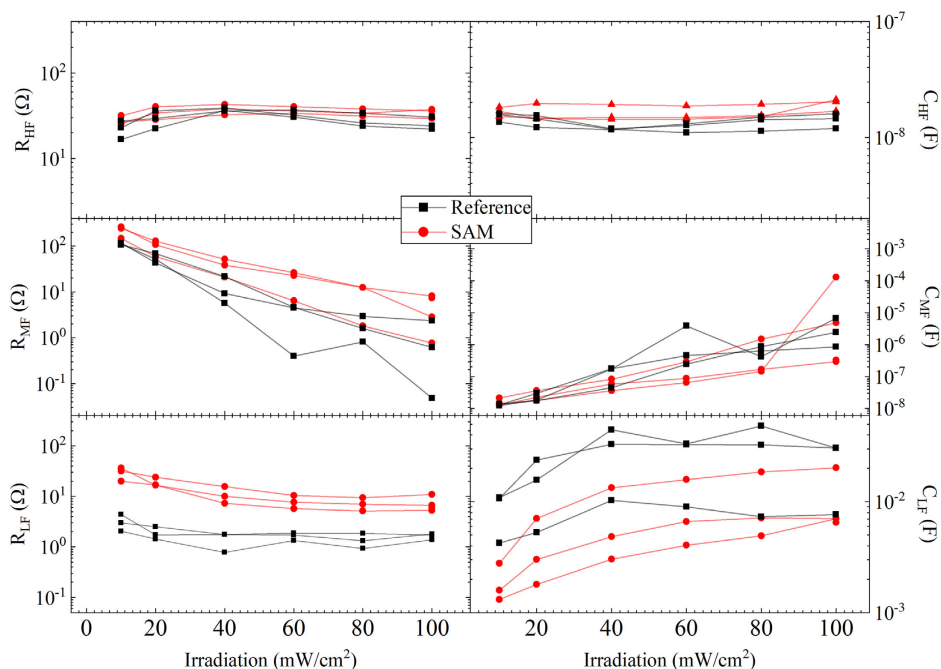


FIGURE 5 | Resistances (left) and capacitances (right) for cells with and without SAM versus light intensity.

3.3 | DC Characterization at Different Temperatures

Figure 6 shows the efficiency normalized to the value at 303 K, V_{OC} obtained from DC measurements at different temperatures, between 253 and 333 K, and the extrapolation of V_{OC} at 0 K (activation energy, E_A). The value obtained for reference cells (1.1 eV) is significantly lower than the energy bandgap (1.6 eV), confirming the presence of a high recombination. On the other hand, activation energy for SAM devices (1.6 eV) matches the energy bandgap, which is indicative of a lower recombination. This could be motivated by a lower presence of mobile ions in the perovskite with SAMs, since ions can behave as localized recombination centers.

As can be observed in Figure 6a, V_{OC} of reference cells is less sensitive to temperature variations than SAM devices, and PCE shows a similar trend. T_{PCE} is defined as the change in PCE with respect to temperature, normalized to the PCE at RT. The obtained value for our devices is $-0.002\% K^{-1}$ for both type of devices, which is in good agreement with similar values found in the literature for devices with similar structure and perovskite composition [17]. This value is not only lower than the values of other traditional photovoltaic technologies, such as silicon ($-0.25\% K^{-1}$), GaAs ($-0.08\% K^{-1}$), or copper indium gallium selenide ($-0.32\% K^{-1}$), but also lower than that of solar cells based on other perovskites such as MAPI ($-0.13\% K^{-1}$) or CsFAMAPbIBr ($-0.08\% K^{-1}$) [38]. This low T_{PCE} value compared to other technologies can be explained by i) the wider bandgap of the perovskite composition (1.6 vs 1.1 eV for silicon), which results in a lower dark carrier density and dark saturation current [39] and ii) the bandgap of perovskite materials increases with temperature [40], which is in contrast to the typical behavior exhibited by most conventional semiconductors. This increase can effectively mitigate losses in V_{OC} , thereby directly enhancing the PCE.

3.4 | AC Characterization at Different Temperatures

IS has been measured at different temperatures (from 253 up to 333 K) and experimental data have been fitted using the

Voigt–Matryoshka circuit. As explained before, the low-frequency arc is associated with ion migration. We have used the temperature dependence of the low-frequency time constant (t_{LF}) to estimate the activation energy for the ion migration. The low-frequency time constant ($\tau_{LF} = R_{LF} \times C_{LF}$) related to the low-frequency arc shows an exponential dependence with the temperature, according to ref. [41] (Equation 1). This equation relates the characteristic time of thermally activated processes with the activation energy (E_{ion}).

$$\tau_{LF} = B T e^{\frac{E_{ion}}{k_B T}} \quad (1)$$

where B is a constant related to the material permittivity and doping density, and k_B is the Boltzmann constant. From the Arrhenius plot (see Figure 7), the ion activation energy of 0.55 eV for both devices has been obtained. Previous works suggest that this value corresponds to the iodine (I^-) ions, since they present a lower activation energy than perovskite cations [5]. The obtained activation energy in these devices almost doubles the value obtained for MAPI-based devices (≈ 0.3 eV), which is in good agreement with a more stable perovskite [5]. Alternatively, recent studies suggest that this activation energy could also be related to the energy level of ionic trap centers [27]. This higher activation energy for iodide ion migration results in lower ionic conductivity which positively improves device stability since ion migration triggers and enhances device degradation [25]. A higher E_{ion} leads to a lower diffusion coefficient (D), according to (Equation 2).

$$D = \frac{\nu_0 d^2}{6} e^{-\frac{E_{ion}}{k_B T}} \quad (2)$$

where ν_0 is the attempt-to-escape frequency of an ionic jump and d is the jump distance [42]. The attempt frequency is assumed to be in the order of $10^{12} s^{-1}$ [43] and a jump distance of 4.49 Å was used [44]. At 300 K, we obtain a diffusion coefficient for ions of the order of $D = 2 \times 10^{-13} cm^2 s^{-1}$, lower than the diffusion coefficient found in literature for halide perovskite anions, ranging from 10^{-9} to $10^{-11} cm^2 s^{-1}$ [5, 41].

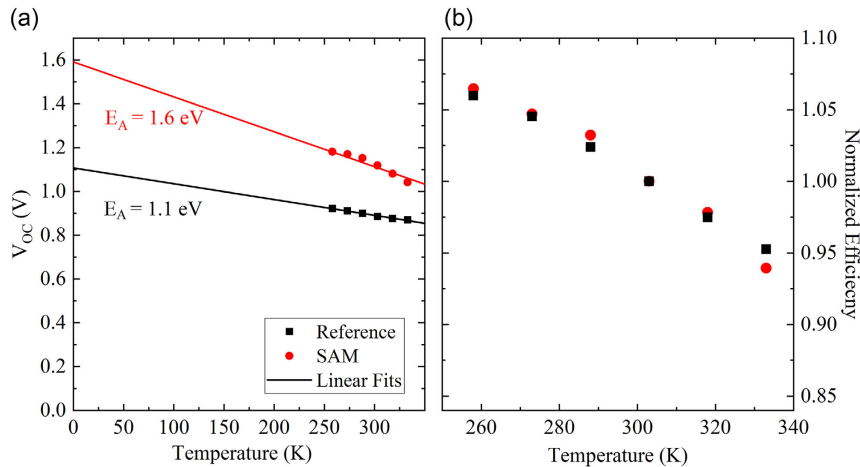


FIGURE 6 | V_{OC} (left) and PCE normalized to the value at 303 K (right) obtained at different temperatures. Recombination activation energy (E_A) has been obtained from the extrapolation of V_{OC} to 0 K.

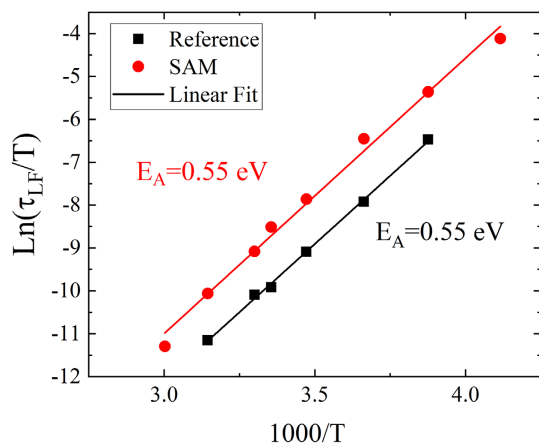


FIGURE 7 | Arrhenius plot $\ln(\tau_{LF}T^{-1})$ versus $1000 T^{-1}$. Symbols show experimental data for SAM (red) and reference (black) cells. Solid lines show the linear fits.

3.5 | Stability

Finally, the impact of incorporating an SAM into the PSC on device stability has been evaluated through an outdoor degradation experiment. Minimodules comprising seven cells connected in series were fabricated and subjected to degradation in accordance with the ISOS-O2 protocol for more than 18 months [28]. Figure 8 illustrates the J_{SC} and efficiency evolution over this period. The data points correspond to the values at maximum daily irradiance, while the lines are visual aid, obtained using a polynomial fit. The evolution of the FF and open-circuit voltage are shown in Figure S2. Two experiments have been carried out, starting in summer 2023 and in autumn 2023. The maximum daytime temperature of the modules is also represented in Figure 8, ranging from 8°C (winter) to 60°C (summer). Results show that, over the long term, modules incorporating SAM exhibit more pronounced degradation compared to those based on the reference structure. T_{80} estimated from the first experiment are around 21 days and 30 days for devices with and without SAM, respectively. This drop in the efficiency is primarily due to a significant decrease in the short-circuit current. The figure shows that this drop is more pronounced during the spring/summer period, especially for SAM devices. Although this behavior could be attributed to the effect of temperature, previous studies [22] conclude that SAM devices were more stable than reference ones under high temperatures in dark conditions. Therefore, it seems that the combination of high temperature and high irradiance (see Figure S3) could be the main cause of the efficiency loss. This stability issue observed in cells containing SAM has been previously reported in refs. [45, 46] and [47] and has been attributed to different causes, such as partial SAM anchoring, desorption of SAM molecules, and diffusion of SAM molecules into the perovskite layer. Although this statement is still a hypothesis, the authors are making progress in researching an optimal methodology to access the degraded perovskite layer without inducing any mechanical stress in the modules.

To ensure a fair comparison, $J-V$ curves of these modules were periodically measured indoors, at 1 sun and at RT, during the degradation experiment. Figure 9 shows the module curves in both the pristine and final states and Table 1 shows the module

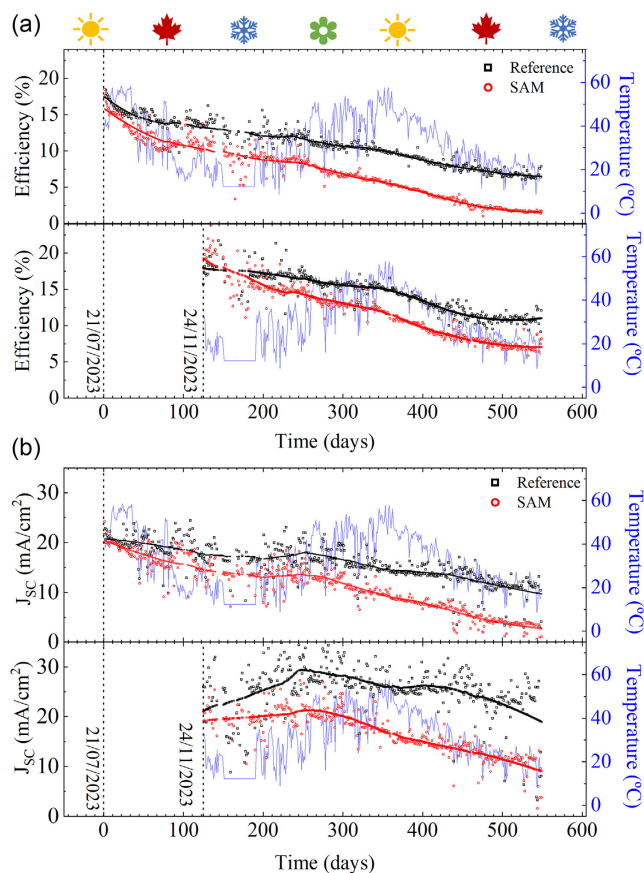


FIGURE 8 | (a) Evolution of efficiency and (b) J_{SC} for the reference and SAM modules. Figures above (below) show the first (second) experiment running from 21st July (24th November) 2023–28th January 2025. Blue line shows the maximum daytime module temperature.

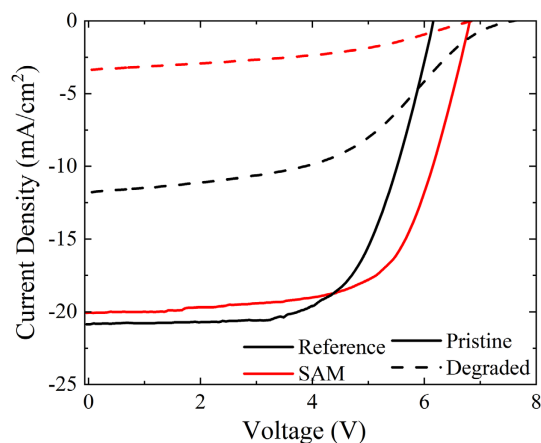


FIGURE 9 | $J-V$ curves of modules, with and without SAM, characterized indoors at 1 sun before and after 550 days under ISOS-O2 degradation protocol.

parameters before and after the ISOS-O2 degradation experiment. Before degradation, J_{SC} of modules exhibits similar values for both structures, while SAM modules display a higher V_{OC} leading to a better efficiency (12.2% vs. 11.2%).

Regarding the degraded devices, the reference cells exhibit an S-shaped curve in the fourth quadrant, which may suggest a

TABLE 1 | Parameters of the modules (with and without SAM) before and after the outdoor degradation experiment starting on 21st July.

Module	J_{SC} (mA cm ⁻²)	V_{OC} (V)	FF	Efficiency (%)
Reference—pristine	19.81	6.16	0.64	11.2
SAM—pristine	19.04	6.82	0.66	12.2
Reference—degraded	11.20	7.59	0.46	5.59
SAM—degraded	3.22	6.86	0.42	1.31

change in the energy level alignment due to interface degradation. This effect is barely observed in the cells with SAM, suggesting that the functional group responsible for improved energy alignment retains its functionality throughout the degradation experiment. On the other hand, the SAM cells exhibit a more significant decrease in short-circuit current, which may indicate unbalanced charge transport in the perovskite. This phenomenon could be attributed to the degradation of the SAM spacer, as this group of the SAM is responsible for the perovskite conductivity [48].

Finally, impedance measurements were also recorded indoors for both modules along the degradation experiment duration. Figure 10 shows the Cole–Cole diagrams at different degradation states (spectra have been fitted using the circuit shown in Figure 4). Inset shows the normalized high-frequency capacitance associated with the geometrical capacitance. The stronger decrease of C_{HF} for SAM modules is attributed to a proportional decrease of the dielectric constant. This trend confirms the hypothesis that SAM modules experience more significant active layer degradation, likely due to the deterioration of the SAM spacer group or the diffusion of SAM along the perovskite active layer.

The hook observed in the low-frequency region of the Cole–Cole diagrams was previously observed and simulated by

P. Cameron [37]. They have attributed this behavior to the cell instability. It is important to emphasize that this low-frequency behavior does not correspond to inductive effects, contrary to what is typically observed in PSCs, as the imaginary part of the impedance remains negative.

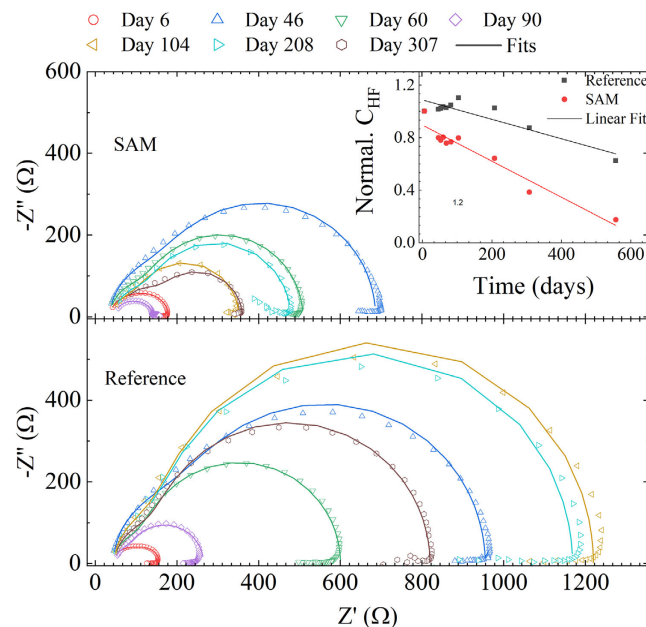
4 | Conclusions

In this work, we have studied inverted PSCs based on double-cation and double-halide perovskite (CsFAPbI₂Br). A comparative analysis was conducted on cells incorporating an SAM between the perovskite and the NiO_x HTL versus reference cells lacking the SAM. Our findings show that the open-circuit voltage is higher in cells incorporating the SAM. This enhancement is attributed to an improved energy level alignment between the valence band of the perovskite and the HOMO of the NiO_x/SAM, consequently leading to an increase in the device efficiency. The ideality factor of devices incorporating the SAM is around 1.4, whereas reference cells exhibit a value less than 1. This indicates that in the absence of the SAM, the contacts are nonselective, leading to charge accumulation at the interface. The incorporation of the SAM improves the quality of the contacts, resulting in recombination predominantly occurring within the bulk.

From the extrapolation of V_{OC} to 0 K, an activation energy of 1.6 eV was obtained for devices with the SAM, which is similar to the perovskite bandgap. In contrast, reference cells exhibited an activation energy of 1.1 eV. This provides further confirmation that recombination primarily occurs in the bulk for devices with the SAM, whereas in reference cells, it occurs at the perovskite/NiO_x interface.

IS measurements were conducted at various temperatures for both devices. An Arrhenius plot of the low-frequency characteristic time constant ($\tau_{LF} = R_{LF} \times C_{LF}$) was used to determine the ion activation energy resulting in the same value of 0.55 eV for both devices. This value can be associated with ions mobility or with the energy level of ionic trap centers and is nearly double the ion activation energy in MAPI perovskite, thereby confirming the enhanced stability of CsFAPbI₂Br compared to standard MAPI.

Finally, an outdoor degradation experiment conducted over a period exceeding 18 months, following ISOS-O2 protocol, with modules based on both layer structures, with and without SAM, reveals that SAM devices exhibit more pronounced degradation due to a significant reduction in the short-circuit current. This phenomenon can be attributed to a substantial deterioration of the SAM spacer and/or to the diffusion of the SAM within the perovskite active layer, which degrades the perovskite active layer.

**FIGURE 10** | Experimental impedance data of SAM (top) and reference (bottom) modules, characterized at different degradation times.

Acknowledgements

This research was funded by *Agencia Estatal de investigación* (projects PID2023-148746OB-I00 and TED2021-131807A-I00) and by the *Universidad Rey Juan Carlos* (project 2023/SOLCON-131819). This research was also partly funded by the fonds wetenschappelijk onderzoek (FWO) with grant number 1S01525N. [Correction added on 25 June 2025, after first online publication: additional affiliation for B. Romero has been added.]

Conflicts of Interest

The authors declare no conflicts of interest.

Data Availability Statement

The data that support the findings of this study are available from the corresponding author upon reasonable request.

References

1. M. A. Green, A. Ho-Baillie, and H. J. Snaith, "The Emergence of Perovskite Solar Cells," *Nature Photonics* 8 (2014): 506, <https://doi.org/10.1038/nphoton.2014.134>.
2. A. Kojima, K. Teshima, Y. Shirai, and T. Miyasaka, "Organometal Halide Perovskites as Visible-Light Sensitizers for Photovoltaic Cells," *Journal of the American Chemical Society* 131 (2009): 6050, <https://doi.org/10.1021/ja809598r>.
3. M. A. Green, E. D. Dunlop, M. Yoshita, et al., "Solar Cell Efficiency Tables (Version 64)," *Progress in Photovoltaics: Research and Applications* 32 (2024): 425–441, <https://doi.org/10.1002/pip.3831>.
4. J. Sun, and J. J. Jasieniak, "Semi-Transparent Solar Cells," *Journal of Physics D: Applied Physics* 50 (2017): 093001, <https://doi.org/10.1088/1361-6463/aa53d7>.
5. M. H. Futscher, J. M. Lee, L. McGovern, et al., "Quantification of Ion Migration in CH₃ NH₃ PbI₃ Perovskite Solar Cells by Transient Capacitance Measurements," *Materials Horizons* 6 (2019): 1497–1503, <https://doi.org/10.1039/C9MH00445A>.
6. Y. Zheng, Y. Li, R. Zhuang, et al., "Towards 26% Efficiency in Inverted Perovskite Solar Cells via Interfacial Flipped Band Bending and Suppressed Deep-Level Traps," *Energy & Environmental Science* 17 (2024): 1153–1162, <https://doi.org/10.1039/D3EE03435F>.
7. H. Zhang, and N.-G. Park, "Progress and Issues in p-i-n Type Perovskite Solar Cells," *DeCarbon* 3 (2024): 100025, <https://doi.org/10.1016/j.decarb.2023.100025>.
8. C. Marchant, and Ré M. Williams, "Perovskite/Silicon Tandem Solar Cells-Compositions for Improved Stability and Power Conversion Efficiency," *Photochemical & Photobiological Sciences* 23 (2024): 1–22, <https://doi.org/10.1007/s43630-023-00500-7>.
9. S. Y. Kim, S. J. Cho, S. E. Byeon, X. He, and H. J. Yoon, "Self-Assembled Monolayers as Interface Engineering Nanomaterials in Perovskite Solar Cells," *Advanced Energy Materials* 10 (2020): <https://doi.org/10.1002/aenm.202002606>.
10. W. Peng et al., "A Versatile Energy-Level-Tunable Hole-Transport Layer for Multi-Composition Inverted Perovskite Solar Cells," *Energy & Environmental Science* 18 (2025): 874–883, <https://doi.org/10.1039/D4EE03208J>.
11. M. Li, M. Liu, F. Qi, F. R. Lin, and A. K.-Y. Jen, "Self-Assembled Monolayers for Interfacial Engineering in Solution-Processed Thin-Film Electronic Devices: Design, Fabrication, and Applications," *Chemical Reviews* 124 (2024): 2138–2204, <https://doi.org/10.1021/acs.chemrev.3c00396>.
12. A. R. M. Alghamdi, M. Yanagida, Y. Shirai, G. G. Andersson, and K. Miyano, "Surface Passivation of Sputtered NiO_x Using a SAM Interface Layer to Enhance the Performance of Perovskite Solar Cells," *ACS Omega* 7 (2022): 12147–12157, <https://doi.org/10.1021/acsomega.2c00509>.
13. G. Kim et al., "Enhancing Surface Modification and Carrier Extraction in Inverted Perovskite Solar Cells via Self-Assembled Monolayers," *Nanomaterials* 14 (2024): 214, <https://doi.org/10.3390/nano14020214>.
14. C. Wu, H. Li, Y. Yan, et al., "Highly-Stable Organo-Lead Halide Perovskites Synthesized Through Green Self-Assembly Process," *Sol. RRL* 2 (2018), <https://doi.org/10.1002/solr.201800052>.
15. D. Yeo et al., "Self-Assembled Monolayer-Based Hole-Transporting Materials for Perovskite Solar Cells," *Nanomaterials* 14 (2024): 175, <https://doi.org/10.3390/nano14020175>.
16. F. Ali, C. Roldán-Carmona, M. Sohail, and M. K. Nazeeruddin, "Applications of Self-Assembled Monolayers for Perovskite Solar Cells Interface Engineering to Address Efficiency and Stability," *Advanced Energy Materials* 10 (2020), <https://doi.org/10.1002/aenm.202002989>.
17. B. Romero, S. Delgado, D. Glowienka, et al., "Highly Stable CsFAPbI₃ Perovskite Solar Cells with Dominant Bulk Recombination at Real Operating Temperatures," *Sustainable Energy & Fuels* 7 (2023): 2146–2152, <https://doi.org/10.1039/D2SE01766K>.
18. T. Wu, L. K. Ono, R. Yoshioka, et al., "Elimination of Light-Induced Degradation at the Nickel Oxide-Perovskite Heterojunction by Aprotic Sulfonium Layers towards Long-Term Operationally Stable Inverted Perovskite Solar Cells," *Energy & Environmental Science* 15 (2022): 4612–4624, <https://doi.org/10.1039/D2EE01801B>.
19. X. Cai, T. Hu, H. Hou, et al., "A Review for Nickel Oxide Hole Transport Layer and Its Application in Halide Perovskite Solar Cells," *Materials Today Sustainability* 23 (2023): 100438, <https://doi.org/10.1016/j.mtsust.2023.100438>.
20. D. Di Girolamo, F. Matteocci, F. U. Kosasih, et al., "Stability and Dark Hysteresis Correlate in NiO-Based Perovskite Solar Cells," *Advanced Energy Materials* 9 (2019), <https://doi.org/10.1002/aenm.201901642>.
21. F. Ma, Y. Zhao, J. Li, X. Zhang, H. Gu, and J. You, "Nickel Oxide for Inverted Structure Perovskite Solar Cells," *Journal of Energy Chemistry* 52 (2021): 393–411, <https://doi.org/10.1016/j.jechem.2020.04.027>.
22. M. Tutundzic, X. Zhang, S. Lammar, et al., "Toward Efficient and Fully Scalable Sputtered NiO_x-Based Inverted Perovskite Solar Modules via Co-Ordinated Modification Strategies," *Sol. RRL* 8 (2024), <https://doi.org/10.1002/solr.202300862>.
23. S. Liu et al., "Buried Interface Molecular Hybrid for Inverted Perovskite Solar Cells," *Nature* 632 (2024): 536–542, <https://doi.org/10.1038/s41586-024-07723-3>.
24. T. Wu, S. Mariotti, P. Ji, et al., "Self-Assembled Monolayer Hole-Selective Contact for Up-Scalable and Cost-Effective Inverted Perovskite Solar Cells," *Advanced Functional Materials* 34 (2024), <https://doi.org/10.1002/adfm.202316500>.
25. L. McGovern, M. H. Futscher, L. A. Muscarella, and B. Ehrler, "Understanding the Stability of MAPbBr₃ versus MAPbI₃: Suppression of Methylammonium Migration and Reduction of Halide Migration," *The Journal of Physical Chemistry Letters* 11 (2020): 7127–7132, <https://doi.org/10.1021/acs.jpcclett.0c01822>.
26. B. Gao and J. Meng, "RbCs(MAFA)PbI₃ Perovskite Solar Cell with 22.81% Efficiency Using the Precise Ions Cascade Regulation," *Applied Surface Science* 530 (2020): 147240, <https://doi.org/10.1016/j.apsusc.2020.147240>.
27. J. Parion, S. Ramesh, S. Subramaniam, et al., "Multifaceted Characterization Methodology for Understanding Nonidealities in Perovskite Solar Cells: A Passivation Case Study," *Sol. RRL* 8 (2024), <https://doi.org/10.1002/solr.202400529>.

28. M. V. Khenkin, E. A. Katz, A. Abate, et al., "Consensus Statement for Stability Assessment and Reporting for Perovskite Photovoltaics Based on ISOS Procedures," *Nature Energy* 5 (2020): 35–49, <https://doi.org/10.1038/s41560-019-0529-5>.
29. X. Zhang, W. Qiu, S. Aperi, et al., "Minimizing the Interface-Driven Losses in Inverted Perovskite Solar Cells and Modules," *ACS Energy Letters* 8 (2023): 2532–2542, <https://doi.org/10.1021/acsenergylett.3c00697>.
30. Y. Wang, J. Ye, J. Song, et al., "Synchronous Modulation of Hole-Selective Self-Assembled Monolayer and Buried Interface for Inverted Perovskite Solar Cells," *Cell Reports Physical Science* 5 (2024): 101992, <https://doi.org/10.1016/j.xcrp.2024.101992>.
31. P. Caprioglio, C. M. Wolff, O. J. Sandberg, et al., "On the Origin of the Ideality Factor in Perovskite Solar Cells," *Advanced Energy Materials* 10 (2020), <https://doi.org/10.1002/aenm.202000502>.
32. W. Tress et al., "Interpretation and Evolution of Open-Circuit Voltage, Recombination, Ideality Factor and Subgap Defect States during Reversible Light-Soaking and Irreversible Degradation of Perovskite Solar Cells," *Energy & Environmental Science* 11 (2018): 151–165, <https://doi.org/10.1039/C7EE02415K>.
33. D. Glowienka and Y. Galagan, "Light Intensity Analysis of Photovoltaic Parameters for Perovskite Solar Cells," *Advanced Materials* 34 (2022), <https://doi.org/10.1002/adma.202105920>.
34. A. Todinova, L. Contreras-Bernal, M. Salado, et al., "Towards a Universal Approach for the Analysis of Impedance Spectra of Perovskite Solar Cells: Equivalent Circuits and Empirical Analysis," *ChemElectroChem* 4 (2017): 2891–2901, <https://doi.org/10.1002/celec.201700498>.
35. J. C. Pérez-Martínez, D. Martín-Martín, G. del Pozo, Bén Arredondo, A. Guerrero, and B. Romero, "Impact of Scan Rate and Mobile Ion Concentration on the Anomalous J-V Curves of Metal Halide Perovskite-Based Memristors," *IEEE Electron Device Letters* 44 (2023): 1276–1279, <https://doi.org/10.1109/LED.2023.3288298>.
36. F. Galatopoulos et al., "The Effect of Hole Transporting Layer in Charge Accumulation Properties of p-i-n Perovskite Solar Cells," *APL Materials* 5 (2017), <https://doi.org/10.1063/1.4991030>.
37. W. Clarke, G. Richardson, and P. Cameron, "Understanding the Full Zoo of Perovskite Solar Cell Impedance Spectra with the Standard Drift-Diffusion Model," *Advanced Energy Materials* 14 (2024), <https://doi.org/10.1002/aenm.202400955>.
38. T. Moot, J. B. Patel, G. McAndrews, et al., "Temperature Coefficients of Perovskite Photovoltaics for Energy Yield Calculations," *ACS Energy Letters* 6 (2021): 2038–2047, <https://doi.org/10.1021/acsenergylett.1c00748>.
39. M. C. López-González, G. del Pozo, Bén Arredondo, et al., "Temperature Behaviour of Mixed-Cation Mixed-Halide Perovskite Solar Cells. Analysis of Recombination Mechanisms and Ion Migration," *Organic Electronics* 120 (2023): 106843, <https://doi.org/10.1016/j.orgel.2023.106843>.
40. Y. A. Olanrewaju et al., "Effects of Temperature-Dependent Burn-in Decay on the Performance of Triple Cation Mixed Halide Perovskite Solar Cells," *AIP Advances* 12 (2022), <https://doi.org/10.1063/5.0078821>.
41. M. H. Futscher et al., "Quantifying Mobile Ions and Electronic Defects in Perovskite-Based Devices with Temperature-Dependent Capacitance Measurements: Frequency Vs Time Domain," *The Journal of Chemical Physics* 152 (2020), <https://doi.org/10.1063/1.5132754>.
42. D. Meggiolaro, E. Mosconi, and F. De Angelis, "Formation of Surface Defects Dominates Ion Migration in Lead-Halide Perovskites," *ACS Energy Letters* 7 (2019): 779–785, <https://doi.org/10.1021/acsenergylett.9b00247>.
43. J. Koettgen, T. Zacherle, S. Grieshammer, and M. Martin, "Ab Initio Calculation of the Attempt Frequency of Oxygen Diffusion in Pure and Samarium Doped Ceria," *Physical Chemistry Chemical Physics* 18 (2017): 9957–9973, <https://doi.org/10.1039/C6CP04802A>.
44. D. W. Ferdani et al., "Opposites Attract, Muons as Direct Probes for Iodide Diffusion in Methyl Ammonium Lead Iodide, (Condensed Matter, Cornell University, 2018), <https://doi.org/10.48550/ARXIV.1801.03845>.
45. H. Guo et al., "Neglected Acidity Pitfall: Boric Acid-Anchoring Hole-Selective Contact for Perovskite Solar Cells," *National Science Review* 10 (2023), <https://doi.org/10.1093/nsr/nwad057>.
46. H. Tang, Z. Shen, Y. Shen, et al., "Reinforcing Self-Assembly of Hole Transport Molecules for Stable Inverted Perovskite Solar Cells," *Science* 386 (2024): 1236–1240, <https://doi.org/10.1126/science.adj9602>.
47. C. Zhang, Z. Yu, B. Li, et al., "Exploring the Potential and Hurdles of Perovskite Solar Cells with p-i-n Structure," *ACS Nano* 18 (2024): 32299–32314, <https://doi.org/10.1021/acsnano.4c11866>.
48. C. E. Puerto Galvis, D. A. González Ruiz, E. Martínez-Ferrero, and E. Palomares, "Challenges in the Design and Synthesis of Self-Assembling Molecules as Selective Contacts in Perovskite Solar Cells," *Chemical Science* 15 (2024): 1534–1556, <https://doi.org/10.1039/D3SC04668K>.

Supporting Information

Additional supporting information can be found online in the Supporting Information section.